Sensitivity of Hurricane Intensity and Structure to Two Types of Planetary Boundary Layer Parameterization Schemes in Idealized HWRF Simulations

Jie Tang[1], Jun A. Zhang[2, 3], Chanh Kieu[4], Frank D. Marks[2]

[1]Shanghai Typhoon Institute, Shanghai, China

[2]NOAA/AOML Hurricane Research Division, Miami, Florida, USA

[3]University of Miami, Cooperative Institute for Marine and Atmospheric Studies, Miami, Florida, USA

[4]Indiana University, Department of Earth and Atmospheric Sciences, Bloomington, Indiana, USA

Abstract

This paper investigates the sensitivity of simulated hurricane intensity and structure to two planetary boundary layer (PBL) schemes in the Hurricane Weather and Research Forecast model including (1) the GFS scheme (control run) that uses the K-profile method to parameterize turbulent fluxes, and (2) the MYJ scheme that is based on turbulent kinetic energy (TKE) budget for turbulent closure. Idealized simulations with these two PBL schemes show that the storm in the TKE run is stronger than that in the control run after three days into simulation. Multi-scale structures are evaluated and compared between the control and the TKE runs prior to the divergence of the model-simulated intensity to elucidate the mechanism underlying such a difference in the intensity between the two runs. It is found that the storm in the TKE run has (i) a shallower boundary layer with a stronger PBL inflow, (ii) stronger boundary layer convergence closer to the storm center, (iii) higher vorticity and inertial stability inside the RMW, (iv) stronger and deeper updrafts in regions further inward from the radius of maximum wind (RMW), and (v) more convective bursts located near the RMW as compared to the control run. Angular momentum budget analysis suggests that the convergence of angular momentum in the boundary layer is much stronger in the TKE run than in the control run, which is responsible for faster spin-up of the hurricane vortex in the TKE run.

1. Introduction

Forecasting hurricane intensity is a challenging problem in the current practice at all hurricane operational centers. This is because hurricane intensity is governed not only by the complex interaction between hurricanes and their atmospheric environment but also by high nonlinearity of hurricane intrinsic dynamics, particularly those in or near the hurricane eyewall.

Thus, more advanced regional/global prediction models are required to accurately represent these processes such that hurricane intensity prediction can be significantly improved. As the model grid spacing is increased to as small as 2 km in the operational regional hurricane models, realistic representation of the sub-grid scale processes such as turbulent transport in the boundary layer or in the eyewall region becomes more crucial for the model development.

Previous theoretical and numerical studies have demonstrated that turbulent processes in the atmospheric boundary layer play an essential role in the maintenance and intensification of hurricanes (e.g., Ooyama 1969; Emanuel 1986; Smith et al. 2009; Bryan 2012; Cione et al. 2013; Montgomery and Smith 2014; Zhang et al. 2017). It is also well-known that simulated hurricane intensity and structure are sensitive to the planetary boundary layer (PBL) schemes that parameterize turbulent fluxes and vertical mixing process in the boundary layer (Braun and Tao 2000; Nolan et al. 2009 a,b; Montgomery et al. 2010; Smith and Thomsen 2010; Kepert 2012; Green and Zhang 2014; Ming and Zhang 2016). However, these studies are based on research models such as the fifth-generation Pennsylvania State University–National Center for Atmospheric Research Mesoscale Model (MM5) or the Weather Research and Forecasting (WRF)–Advance Research WRF (ARW) instead of operational hurricane forecast models such as the Hurricane Weather and Research Forecast (HWRF) model.

Given the importance of improving hurricane intensity forecast for operational purposes, the Hurricane Forecast Improvement Project (HFIP) has been initiated in 2009 by the National Oceanic and Atmospheric Administration (NOAA) and since then provided the basis for NOAA and other agencies to coordinate hurricane research needed to improve hurricane models (Gall et al. 2013). Efforts have been made to improve the operational HWRF model during the tenure of HFIP from different perspectives including development of model vortex initialization through

data assimilation, optimization of the model horizontal and vertical resolution, implementation of new hurricane physics based on observations, and upgrades of operational and diagnostic products.

This study is a follow-up of our previous work on evaluating and improving the boundary layer physics of the HWRF model (e.g., Zhang et al. 2015). The approach used in our previous studies (Zhang et al. 2012; Gopalakrishnan et al. 2013) focused on improving a single planetary boundary layer (PBL) scheme in the HWRF model, the so-called GFS scheme which is essentially the Medium Range Forecast (MRF) scheme. Here, we evaluate the performance of a different PBL scheme, the so-called the TKE-based scheme with higher order turbulent closure, in HWRF to gain more understanding into how other types of PBL scheme behave in HWRF. This evaluation is of considerable importance in the HWRF model development, as it will provide guidance on which PBL parameterization scheme that one should implement in the future model upgrade.

2. Model Simulations and Analysis Method

In this work, we use the triply-nested version of HWRF in an idealized framework (Gopalakrishnan et al. 2013). The parent domain of the model that covers an area of 50×50 degrees is designed with a coarse grid spacing of 27 km, along with two two-way interaction inner nests that have horizontal resolution of 9 km and 3 km, and cover an area of ~15 $\times$ 15 degrees and ~5 $\times$ 5 degrees, respectively. The model has 42 hybrid vertical levels with more than 10 levels below the 850-hPa level. The model is initialized by solving the non-linear balance equation in the pressure-based sigma coordinate system on an f-plane centered at 15°N following Wang (1995). The initial axisymmetric cyclonic vortex has a maximum wind speed of 20 m s^{-1}

and a radius of maximum wind speed of about 90 km, and is embedded in a quiescent environment. For simplicity, in all of the experiments, the environmental temperature and humidity fields were from Jordan's Caribbean sounding (Jordon 1958); the sea surface temperature was set to a constant of 302 K and no land exists anywhere in the three domains.

The model physics options used in this study were configured as close as possible to the operational HWRF in a similar manner as in Gopalakrishnan et al. (2013). Specifically, our description of the model physics below parallels that in Gopalakrishnan et al. (2013). Surface fluxes are parameterized using the exchange coefficients based on recent observational studies from the field and laboratory experiments (Zhang et al. 2008; Haus et al. 2010; Bell et al. 2012). The drag coefficient (C_d) under the neutral condition is parameterized through the surface roughness length (z_0). Details of the surface layer parameterization in HWRF are given by Zhang et al. (2015). The Geophysical Fluid Dynamics Laboratory (GFDL) long wave radiation scheme following Fels and Schwarzkopf (1975) and Schwarzkopf and Fels (1991), as well as the short-wave radiation scheme of Lacis and Hansen (1974) were used. For microphysics parameterization, the Ferrier scheme (Ferrier et al. 2002) is used. It should be noted that the Simplified Arakawa and Schubert scheme (SAS, Pan and Wu 1995; Hong and Pan 1998) for convective parameterization is used only for the two outermost and intermediate domains at resolutions of 27 km and 9 km following Gopalakrishnan et al. (2013). For the horizontal diffusion, HWRF uses a first order nonlinear Smagorinsky-type parameterization (Janjic 1990). Details of the horizontal diffusion parameterization in HWRF is given by Zhang and Marks (2015).

Because the main focus in this study is on the PBL parameterization schemes, we conducted two experiments using two different types of PBL schemes to investigate the effect of

PBL parameterization on TC intensity and structure. The first PBL scheme currently used in the

operational HWRF model is called 'GFS' scheme in the HWRF community. This scheme is

essentially the modified Medium Range Forecast (MRF) scheme (Troen and Marht, 1986; Hong

and Pan 1996). In this scheme, turbulent fluxes are parameterized using the vertical eddy

diffusivity (K_m) that has the form of:

$$K_m = k \, (u*/F) \, z \, \{\alpha \, (1 - z/h)^2\},\tag{1}$$

where $\kappa = 0.4$ is the Von Karman constant, $u*$ is the surface frictional velocity, F is the stability

function evaluated at the top of the surface layer, z is the height above the surface, and h is the

boundary layer height that is calculated as the height at which the bulk Richardson number is

greater than a critical value. Here, α is a tuning parameter which is parameterized based

observational data given by Zhang et al. (2011a). The vertical eddy diffusivity for momentum,

heat and moisture are set to be the same.

   The other PBL scheme is the Mellor-Yamada-Janjic (MYJ) scheme, which is an updated

version of the original Mellor-Yamada boundary layer parameterization (Mellor and Yamada

1974, 1982) that was implemented for use in numerical weather prediction by Janjic (1990), such

as in the Weather and Research Forecast (WRF) model. The MYJ scheme predicts the

generation and redistribution of turbulent kinetic energy (TKE) in the boundary layer. In the

MYJ scheme, it is noted that the TKE, the local vertical gradients of mean quantities, and the

diagnosed length scale are used to compute the vertical eddy diffusivity for momentum heat and

moisture in the form of:

$$K_m = c \, l \, e^{1/2},\tag{2}$$

where c is the coefficient which a function of flux Richardson number, e is the TKE, and l is the mixing length which is defined as

$$\frac{1}{l} = \frac{1}{kz} + \frac{1}{\delta} \tag{3}$$

where κ is Von Karman constant and $\kappa = 0.4$, z is the altitude, and δ is the asymptotic mixing length.

For the purpose of comparison between the two PBL schemes, all the experiments are conducted with the same initialization and physics options except for the PBL scheme. Hereafter, the simulation with the GFS scheme is referred to as the control run (CTL) and that with the MYJ scheme is referred to as the TKE run.

3. Results

To have a first picture of the model behaviors for different PBL scheme, the maximum surface wind speed (VMAX) during the 5-day integration of the two experiments as a function of simulated time is shown **Fig. 1**. One notices in this time series that VMAX is almost same for the two runs during the first 36 h (i.e., the spin-up period). After that time, the model intensity in the control run varies strongly between 34 and 47 m s^{-1}, while the intensity in the TKE run stays nearly steady up to 72 h and then increases rapidly with time. Although the difference in the intensity between the two runs is generally small up to 72 h, the difference in the maximum intensity is as large as 15 m s^{-1} at the end of the 5-day simulation. Although the two runs share similar rapid intensification during the first 48 h, the mean intensification rate is significantly different after 72 h as shown in **Fig. 1**, with the storm in the TKE run intensifying faster than that in the control run.

6

The difference in the maximum azimuthally averaged tangential (V_t) and radial (V_r) velocities between the CTL and the TKE runs, which represent the axisymmetric structure of the model vortex, is more clearly shown than that in the point-like VMAX metric (**Figs. 2a** and **2b**). Prior to 48 h, the maximum V_t and minimum V_r are close to each other for the two runs, but they evolve with different trends after this time. Specifically, both the maximum V_t and minimum V_r In the CTL run stay nearly constant with time after 48 h, while their magnitudes increase with time in the TKE run. On the other hand, the simulated inner-core size is essentially same between the two runs, except that the CTL storm has a slightly larger RMW after 96 h of simulation (**Fig. 2c**). Note that in both experiments, the HWRF model could capture the cessation of the RMW contraction at the middle of rapid intensification, i.e. around 24 h, similar to what reported in both idealized experiments (Kieu 2012; Stern et al. 2015).

The radius-height representation of the azimuthally-averaged V_t is shown in **Figs. 3a** and **3b** for the two simulations, which is averaged between 48-72 h, when the simulated storm is in a nearly steady-state phase before t = 72 h after which the model intensity shows a large divergence. Of interest is the emergence of a V_t maximum known as the boundary-layer jet, which is located at ~35 km radius and ~700 m altitude in both simulations. This "azimuthal jet" structure, which is one of the distinct features that are different from a typical boundary layer in non-TC conditions, is similar to that found in previous observational and numerical studies (e.g., Kepert 2001; Franklin et al. 2003; Kepert 2006a,b; Bell and Montgomery 2008; Nolan et al. 2009b; Zhang et al. 2011b; Mongomery et al. 2014; Rogers et al. 2015). The peak V_t in the CTL run is 46 m s^{-1}, which is smaller than that (42 m s^{-1}) in the TKE simulation. The height of the maximum V_t denoted by the black dashed line decreases with decreasing radius in both simulations, in agreement with observational composite analyses in Zhang et al. (2011b). This

kinematic boundary layer height is slightly larger inward from ~100 km towards the storm center in the control run than in the TKE run. Such a difference in the kinematic PBL height is attributed to the fact that the K_m parameterization given by Eq. (2) is a more sensitive function of the storm structure. Thus, the PBL height in the TKE scheme quickly reduces inwards from $r = 130$ km (**Fig. 3b**), whereas the PBL height in the control run is nearly constant down to $r \sim 90$ km (**Fig 3a**).

Figures **3c** and **3d** show the azimuthally-averaged V_r as a function of radius and altitude, which is obtained from an average between 48-72 h for the two simulations. The peak radial inflow is found to be located ~150 m above the surface with its magnitude decreasing gradually with height consistent with the observations of Zhang et al. (2011b). The inflow layer depth, defined as the height of 10% peak inflow following Zhang et al. (2011b), tends to decrease with decreasing radius to the storm center, which is also consistent with observations. One notices from **Figs. 3c** and **3d**, however, a key difference that the peak inflow in the TKE run is much larger than that in the CTL run. In addition, the outflow above the inflow layer is also substantially stronger in the TKE run than in the control run, while the TKE inflow layer is shallower than that in the control run.

Comparison of the vortex-scale structure between the two runs, represented by the azimuthally averaged relative vorticity, is provided in **Fig. 4**. One notices that the relative vorticity in the TKE run is substantially larger than that in the CTL run as expected from the stronger VMAX towards the end of the 5-day simulation, especially inside the RMW. Furthermore, the relative vorticity inside the RMW is larger almost throughout the troposphere in the TKE run than that in the CTL run, indicating that both the lower-level and upper-level vortices spin up faster in the TKE run. Physically, this larger relative vorticity in the TKE is

mostly related to the stronger frictional convergence implied by the shallower PBL height (**Fig. 3b**) and the stronger peak inflow seen in **Fig. 3d**.

Figure 5 compares the azimuthally averaged vertical velocity (w) and low-level divergence/convergence between the two runs. It is evident from **Fig. 5** that the maximum azimuthally-averaged vertical motion w is located at a higher altitude in the TKE run (~ 8 km) than in the CTL run (~ 5 km), with the maximum value of $w \sim 1.5$ m s^{-1} also being much larger in the TKE run. In particular, it is somewhat intriguing to notice that the maximum w is located inward from the RMW (indicated by the black line with a near up-right position) in the TKE run, while it is located almost at the same RMW radius in the CTL run. Consistent with this vertical motion distribution, the boundary layer convergence is found to be much larger in the TKE run than in the CTL run, so is the divergence immediately above the boundary layer. From the dynamical standpoint, this coupled structure between convergence/divergence and vertical velocity indicates the consistency of the mass continuity that is initiated from the boundary layer convergence (Ooyama 1969; Shapiro and Willoughby 1982). The peak boundary layer convergence is located slightly inward to the storm center in the TKE run than in the control run. This result (**Fig. 5**) also indicates the ability of convection to ventilate mass at the rate that is converging in the boundary layer (Kilroy et al. 2016).

The importance of deep convection near the RMW for hurricane intensification has been in fact documented in numerous observational and modeling studies (e.g., Vigh and Schubert 2009; Guimond et al. 2010; Rogers et al. 2013). The representation of convection can be evaluated using contoured frequency by altitude diagrams (CFAD) of vertical velocity w, which shows the vertical variation of the distribution of w (Yuter and Houze 1995). Previous studies by, e.g., Rogers et al. (2007), Nolan et al. (2013), and Zhang et al. (2015), showed that CFDA between

the HWRF model and observations is significantly different. **Figures 6a** and **6b,** respectively, show CFADs of *w* in the eyewall region (0.75-1.25 x RMW) for the CTL and TKE runs. It appears that the strongest updrafts (i.e., top $0.1 – 0.3\%$ of the distributions of *w*>5 m s) are more frequent in the TKE run than in the control run. There are more strong updrafts in the TKE run above the boundary layer. As mentioned earlier, this result from the CFADs suggests that deep convection is linked to the vortex intensification, by ventilating mass of air converging in the boundary layer. In the TKE run, since the deep convection is weak, the residual mass flowing out just above the boundary layer could cause a spin-down of the model vortex as discussed in Kilroy et al. (2016).

To further examine the difference of the control and the TKE experiment around the instant at which VMAX in the two runs shows large divergence (i.e., t=72 h), counts of convective bursts[1] 10 h before this bifurcation point in intensity as a function of radius to the storm center normalized by the RMW at 2 km are shown in **Figs. 7a** and **7b,** for the CTL and TKE runs, respectively. It appears that the majority of the bursts are located at the RMW (0.75-1.2 RMW) for the TKE run, but most of the bursts are either located at the RMW or outside the eyewall (~3 RMW) in the control run. This result is consistent with Rogers et al. (2013) and Zhang et al. (2017) who found that the bursts tend to locate at the location near the RMW for intensifying group of storms whereas the bursts tend to locate away from the RMW from the center for steady-state group based on Doppler radar data. This result suggests that the boundary layer structure is strongly coupled with the deep convection.

---

[1] Here a convective burst is defined as a grid point with its maximum vertical motion > 3 m s^{-1} above 8 km altitude.

The azimuthally averaged inertial stability during the same period (t=48-72 h) is shown in **Figs. 7c** and **7d**, respectively, for the control and TKE runs. The peak of the inertial stability is located at ~ 0.5 RMW in the boundary layer for both runs. We note that the inertial stability is larger in the CTL run inward of the RMW (~0.7 – 1 RMW), which is located at roughly 6 km altitude. Despite this difference, the vertical and horizontal distribution of the azimuthally averaged inertial stability in the CTL and TKE runs are quite consistent with the Doppler radar composites given by Rogers et al. (2013) for steady-state and intensifying storms, respectively. This result also agrees with HWRF forecasts shown by Zhang et al. (2017) that examined the effect of vertical eddy diffusivity on TC intensification. It is evident from **Fig. 7** that the bursts (i.e., deep convection) are located at locations of higher inertial stability in the TKE run than in the CTL run, where energy from the latent heat release would be transferred more efficiently to kinetic energy according to theoretical work given by Nolan et al. (2007).

To further understand the dynamics that is responsible for the difference in the intensity between the two experiments, we follow Zhang and Marks (2015) and analyze the budget of the absolute angular momentum defined as $= rV_t + fr^2/2$, where r is radial distance and f is the Coriolis frequency). The description of the angular momentum budget below parallels that of Zhang and Marks (2015), which showed that the budget equation of the azimuthally-averaged M tendency is given by

$$\frac{\partial <M>}{\partial t} = - <V_r> \frac{\partial <M>}{\partial r} - <w> \frac{\partial <M>}{\partial z} - <V_r' \frac{\partial M'}{\partial r}> - <w' \frac{\partial M'}{\partial z}> + F_r, \qquad (4)$$

where the brackets represent azimuthal averages at a constant height, and the primes denote a departure from the azimuthal mean (or et below parallels that of Zhang and Mark) are storm relative. The terms on the right-hand side of Eq. (1) are, respectively, the mean radial advection

of $<M>$, the mean vertical advection of $<M>$, the radial advection of the resolvable eddy angular momentum, the vertical advection of the resolvable eddy angular momentum, and the combined diffusive and boundary layer tendency[2] (F_r).

Figure 8 shows time averages of the terms in the azimuthally-averaged angular momentum Eq. (4) during the period before the intensity bifurcation point (between 48-72 h) for two simulations. The $<M>$ tendency is found to be larger in the eyewall region in the TKE run (**Figs. 8a** and **8b**), which is consistent with the trend of intensity change shown in **Fig. 1**. In both simulations, the total mean advection of $<M>$ and the F_r terms are the main source and sink terms for the tendency of $<M>$, respectively (**Figs. 8c, 8d** and **Figs. 9g, 9h**), which are similar in structure but have an opposite sign. The spin-up of the vortex in the boundary layer is mainly due to the positive mean advection of $<M>$, consistent with Smith et al. (2009). It is evident from **Figs. 8c** and **8d** that the mean advection of $<M>$ in the TKE run is much larger than that in the control run, which explains why the storm in the TKE run intensifies faster than that in the CTL run, given the same eddy advection of $<M>$ between these two runs (**Figs. 8e** and **8f**). Note however that the friction term is also larger in the TKE run than in the control run due to the shallowed PBL height (cf. **Fig. 3b**). Despite this larger fictional term in the TKE run, the net tendency of $<M>$ is overall still larger in the TKE run. Consistent with previous studies, it is seen in both experiments that the mean advection of $<M>$ is indeed mainly from the horizontal mean advection component or the convergence of $<M>$, especially in the boundary layer.

---

[2]The F_r term is the combination of the vertical and horizontal diffusion caused by sub-grid processes.

4. Summary

This study investigates the sensitivity of simulated hurricane intensity and structure to two different types of the PBL schemes in the HWRF model, with one scheme based on the K-profile method, and the other based on the TKE budget method. This work is part of a series of recent studies that employed the idealized configuration of the operational HWRF model to understand the impact of model physics on hurricane intensity and structure simulations (Bao et al. 2012; Gopalakrishnan et al. 2013; Kieu et al. 2014; Zhang and Marks 2015). In this study, idealized simulations with the two PBL schemes, referred to as control run and TKE run, are respectively conducted and analyzed. The results show that the storm in the TKE run is significantly stronger than that in the CTL run after three days into integration. Multi-scale structures are then compared between these two runs to elucidate structural differences that are responsible for the different intensification after the two runs start showing a substantial divergence in the model intensity.

First, it is found that although the storm size is found to be similar in these two simulations, the kinematic boundary layer height is noticeably smaller in the TKE run is than in the CTL run. Corresponding to this shallower PBL depth, the strength of the boundary layer inflow and boundary layer convergence are much stronger in the TKE run than in the control run. Second, the location of the peak convergence is found to be located at the radius closer to the storm center in the TKE run. Analyses of convective bursts during the period prior to the intensity divergence reveal that there are more convective bursts inside the eyewall region in the TKE run than those seen in the control run. Stronger updrafts are also found in the TKE runs inward from the RMW, which are collocated with higher inertial stability. These structural differences are consistent with previous observational studies (e.g., Rogers et al. 2013, 2015,

2016; Zawislak et al. 2016), theoretical studies (Nolan et al. 2007; Vigh and Schubert 2009), and numerical studies (Smith et al. 2017; Zhang et al. 2017; Leighton et al. 2018), thus explaining why the storm in the TKE run tends to intensify faster, given the simulated vortex-scale and convective-scale structural differences. Furthermore, the angular momentum budget analysis suggests that the convergence of angular momentum in the boundary layer is indeed much stronger in the TKE run than in the control run. Our result is also consistent with the hurricane spin-up theory revisited by Smith et al. (2009) that emphasized on the boundary layer mechanism.

While it is still an open question of which PBL scheme will be better suited for hurricane simulations for practical applications, our analyses could show at least that the TKE scheme results in an expected vortex structure similar to what has been obtained from previous observational studies. As part of HFIP, this work is one of several ongoing efforts to evaluate and improve the physical parameterizations of the operational hurricane model (e.g., HWRF). In this regard, this work can provide useful guidance for upgrading the PBL physics in the HWRF model in upcoming implementation. Our future work will focus on model diagnostics of the HWRF simulations for real storms with different PBL schemes to help further understand the roles of PBL schemes in hurricane intensity and forecasts.

References

Bao, J.-W., S. G. Gopalakrishnan, S. A. Michelson, F. D. Marks, Jr., and M. T. Montgomery, 2012: Impact of physics representations in the HWRFX on simulated hurricane structure and pressure–wind relationships. *Mon. Wea. Rev.*, **140**, 3278–3299.

Bell, M. M., and M. T. Montgomery, 2008: Observed structure, evolution, and potential intensity of category 5 Hurricane Isabel (2003) from 12 to 14 September. *Mon. Wea. Rev.*, **136**, 2023–2046.

Bell, M. M., M. T. Montgomery, and K. A. Emanuel, 2012: Air-sea enthalpy and momentum exchange at major hurricane wind speeds observed during CBLAST. *J. Atmos. Sci.*, **69**, 3197–3222.

Bender, M. A., I. Ginis, R. E. Tuleya, B. Thomas, and T. Marchok, 2007: The operational GFDL coupled hurricane–ocean prediction system and a summary of its performance. *Mon. Wea. Rev.*, **135,** 3965–3989.

Braun, S. A., and W.-K. Tao, 2000: Sensitivity of high-resolution simulations of Hurricane Bob (1991) to planetary boundary layer parameterizations. *Mon. Wea. Rev.*, **128**, 3941–3961.

Bryan, G. H., 2012: Effects of surface exchange coefficients and turbulence length scales on the intensity and structure of numerically simulated hurricanes. *Mon. Wea. Rev.,* **140**, 1125–1143.

Bu, Y. P., R. G. Fovell, and K. L. Corbosiero, 2017: The influences of boundary layer vertical mixing and cloud-radiative forcing on tropical cyclone size. *J. Atmos. Sci.,* **74**, 1273–1292.

Cione, J. J., E. A. Kalina, J. A. Zhang, and E. W. Uhlhorn, 2013: Observations of air–sea interaction and intensity change in hurricanes. *Mon. Wea. Rev.*, **141**, 2368–2382.

Emanuel, K. A., 1995: Sensitivity of tropical cyclones to surface exchange coefficients and a revised steady-state model incorporating eye dynamics. *J. Atmos. Sci.,* **52,** 3969-3976.

Gall, R., J. Franklin, F. Marks, E. N. Rappaport, and F. Toepfer, 2013: The Hurricane Forecast Improvement Project. *Bull.Amer.Meteor. Soc.,* **94**, 329–343.

Gopalakrishnan, S. G., F. D. Marks, Jr, J. A. Zhang, X. Zhang, J.-W. Bao and V. Tallapragada, 2013: A study of the impacts of vertical diffusion on the structure and intensity of the tropical cyclones using the high resolution HWRF system. *J. Atmos. Sci.*, **70**, 524–541.

Green, B. W., and F. Zhang, 2014: Sensitivity of tropical cyclone simulations to parametric uncertainties in air–sea fluxes and implications for parameter estimation. *Mon. Wea. Rev.*, **142**, 2290–2308.

Fels, S. B., and M. D. Schwarzkopf, 1975: The simplified exchange approximation: A new method for radiative transfer calculations. *J. Atmos. Sci.*, **32**, 1475–1488.

Ferrier, B. S., Y. Lin, T. Black, E. Rogers, and G. DiMego, 2002: Implementation of a new grid-scale cloud and precipitation scheme in the NCEP Eta model. Preprints, 19th Conf. on

Weather Analysis and Forecasting/15th Conf. on Numerical Weather Prediction, San

Antonio, TX, Amer. Meteor. Soc., 10.1. [Available online at

https://ams.confex.com/ams/SLS_WAF_NWP/techprogram/paper_47241.htm.]

Guimond, S. R., G. M. Heymsfield, and F. J. Turk, 2010: Multiscale observations of Hurricane

Dennis (2005): The effects of hot towers on rapid intensification. *J. Atmos. Sci.*, **67**, 633–

654, doi:10.1175/2009JAS3119.1.

Haus, B. K., D. Jeong, M. A. Donelan, J. A. Zhang, and I. Savelyev, 2010: Relative rates of sea-

air heat transfer and frictional drag in very high winds. *Geophys. Res. Lett.*, **37**, L07802,

doi:10.1029/2009GL042206.

Hong, S.-Y., and H.-L. Pan, 1996: Nonlocal boundary layer vertical diffusion in a medium-range

forecast model. *Mon. Wea. Rev.*, **124**, 2322–2339.

Janji_c, Z. I., 1990: The step-mountain coordinate: Physical package. *Mon. Wea. Rev.*, **118**,

1429–1443.

Kepert, J. D., 2001: The dynamics of boundary layer jets within the tropical cyclone core. Part I:

Linear theory. *J. Atmos. Sci.,* **58**, 2469–2484.

Kepert, J. D, 2012: Choosing a boundary layer parameterization for tropical cyclone modelling.

Mon. Wea. Rev., **140**, 1427–1445.

Kepert, J. D., and Y. Wang, 2001: The dynamics of boundary layer jets within the tropical

cyclone core. Part II: Nonlinear enhancement. *J. Atmos. Sci.*, **58**, 2485–2501.

Kieu, C. Q., 2012: An investigation into the contraction of the hurricane radius of maximum

wind. *Meteor. Atmos. Phys.*, **115**, 47–56.

Kieu, C. Q., V., Tallapragada, and W. Hogsett, 2013: On the onset of the tropical cyclone rapid
intensification in the HWRF model. *Geophys. Res. Lett*., **9**, 3298–3306.

Kilroy, G., R. K. Smith, and M. T. Montgomery, 2016: Why do model tropical cyclones grow
progressively in size and decay in intensity after reaching maturity? *J. Atmos. Sci*., **73**,
487–503.

Lacis, A. A., and J. E. Hansen, 1974: A parameterization for the absorption of solar radiation in
the Earth's atmosphere. *J. Atmos. Sci.,* **31**, 118–133.

Leighton, H., S. Gopalakrishnan, J.A. Zhang, R.F. Rogers, Z. Zhang, and V. Tallapragada, 2018:
Azimuthal distribution of deep convection, environmental factors, and tropical cyclone
rapid intensification: A perspective from HWRF ensemble forecasts of Hurricane
Edouard (2014). *J. Atmos. Sci*., **75**, 275–295.

Ming, J., and J. A. Zhang, 2016: Effects of surface flux parameterization on the numerically
simulated intensity and structure of Typhoon Morakot (2009). *Adv. Atmos. Sci.*, **33**, 58–
72, doi:https://doi.org/10.1007/s00376-015-4202-z.

Montgomery, M. T., and R. K. Smith, 2014: Paradigms for tropical cyclone intensification. *Aust.
Meteor. Oceanogr. J.*, **64**, 37–66.

Montgomery, M. T., R. K. Smith, and S. V. Nguyen, 2010: Sensitivity of tropical cyclone
models to the surface exchange coefficients. *Quart. J. Roy. Meteor. Soc.*, **136**, 1945–
1953, doi:https://doi.org/10.1002/qj.702.

Montgomery, M.T., J. A. Zhang, and R.K. Smith, 2014: An analysis of the observed low-level
structure of rapidly intensifying and mature Hurricane Earl, 2010: *Quart. J. Roy. Meteor.
Soc.,* **140**, 2132-2146.

Nolan, D. S., R. Atlas, K. T. Bhatia, and L. R. Bucci, 2013: Development and validation of a hurricane nature run using the Joint OSSE Nature Run and the WRF model. *J. Adv. Earth. Model. Syst.,* **5**, 1–24.

Nolan, D. S., Y. Moon, and D. P. Stern, 2007: Tropical cyclone intensification from asymmetric convection: energetics and efficiency. *J. Atmos. Sci.*, **64**, 3377–3405.

Nolan D. S., J. A. Zhang, and D. P. Stern, 2009a: Evaluation of planetary boundary layer parameterizations in tropical cyclones by comparison of in-situ data and high-resolution simulations of Hurricane Isabel (2003). Part I: Initialization, maximum winds, and outer core boundary layer structure. *Mon. Wea. Rev.*, **137,** 3651–3674.

Nolan D. S., D. P. Stern, and J. A. Zhang, 2009b: Evaluation of planetary boundary layer parameterizations in tropical cyclones by comparison of in-situ data and high-resolution simulations of Hurricane Isabel (2003). Part II: Inner core boundary layer and eyewall structure. *Mon. Wea. Rev.*, **137,** 3675–3698.

Ooyama, K. V., 1969: Numerical simulation of the life cycle of tropical cyclones. *J. Atmos. Sci.,* **26**, 3–40.

Pan, H.-L., and J. Wu, 1995: Implementing a mass flux convection parameterization package for the NMC Medium-Range Forecast model. NMC Office Note 409, 40 pp. [Available from NCEP, 5200 Auth Road, Washington, DC 20233.]

Pattanayak, S., U. C. Mohanty, and S. G. Gopalakrishnan, 2012: Simulation of very severe Cyclone Mala over Bay of Bengal with HWRF modeling system. *Nat. Hazards*, **63**, 1413–1437.

Reasor, P. D., M. Eastin, and J. F. Gamache, 2009: Rapidly intensifying Hurricane Guillermo (1997). Part I: Low-wavenumber structure and evolution. *Mon. Wea. Rev.*, **137**, 603–631.

Rogers, R.F., M.L. Black, S.S. Chen, and R.A. Black, 2007: An Evaluation of Microphysics Fields from Mesoscale Model Simulations of Tropical Cyclones. Part I: Comparisons with observations. *J. Atmos. Sci.*, **64**, 1811–1834.

Rogers, R., P. Reasor, and S. Lorsolo, 2013: Airborne Doppler observations of the inner-core structural differences between intensifying and steady-state tropical cyclones. *Mon. Wea. Rev.*, **141**, 2970–2991.

Rogers, R. F., P. D. Reasor, and J. A. Zhang, 2015: Multiscale structure and evolution of Hurricane Earl (2010) during rapid intensification. *Mon. Wea. Rev.*, **143**, 536–562.

Rogers, R. F., J. A. Zhang, J. Zawislak, H. Jiang, G. R. Alvey, E. J. Zipser, and S. N. Stevenson, 2016: Observations of the structure and evolution of Hurricane Edouard (2014) during intensity change, Part II: Kinematic structure and the distribution of deep convection. *Mon. Wea. Rev.*, **144**, 3355–3376, doi:10.1175/MWR-D-16-0017.1

Shapiro, L. J., and H. E. Willoughby, 1982: The response of balanced hurricanes to local sources of heat and momentum. *J. Atmos. Sci.*, **39**, 378–394.

Schubert, W. H., M. T. Montgomery, R. K. Taft, T. A. Guinn, S. R. Fulton, J. P. Kossin, and J. P. Edwards, 1999: Polygonal eyewalls, asymmetric eye contraction, and potential vorticity mixing in hurricanes. *J. Atmos. Sci.*, **56**, 1197–1223.

Smith, R. K., and G. L. Thomsen, 2010: Dependence of tropical-cyclone intensification on the boundary layer representation in a numerical model. *Quart. J. Roy Meteor. Soc.*, **136**, 1671-1685.

Smith, R. K. and M. T. Montgomery, 2016: The efficiency of diabatic heating and tropical cyclone intensification. *Quart. J. Roy. Meteor. Soc.*, 142, 2081–2086.

Smith, R. K., M. T. Montgomery, and S. V. Nguyen, 2009: Tropical cyclone spin-up revisited. *Quart. J. Roy Meteor. Soc.,* 135, 1321–1335.

Smith, R. K., J. A. Zhang, and M. T. Montgomery, 2017: The dynamics of intensification in an HWRF simulation of Hurricane Earl (2010). *Quart. J. Roy. Meteor. Soc.*, **143,** 297–308.

Troen, I., and L. Mahrt, 1986: A simple model of the atmospheric boundary layer: Sensitivity to surface evaporation. *Bound.-Layer Meteor.*, **37**, 129–148.

Vigh, J. L. and W. H. Schubert, 2009: Rapid development of the tropical cyclone warm core. *J. Atmos. Sci.*, **66**, 3335–3350.

Yuter, S. E., and R. A. Houze Jr., 1995: Three-dimensional kinematic and microphysical evolution of Florida cumulonimbus. Part III: Vertical mass transport, mass divergence, and synthesis. *Mon. Wea. Rev.*, **123**, 1964–1983.

Zawislak, J.G., H. Jiang, G. R. Alvey, E. J. Zipser, R. F. Rogers, J. A. Zhang, and S. N. Stevenson, 2016: Observations of the structure and evolution of Hurricane Edouard (2014) during intensity change, Part 1: Relationship between the thermodynamic structure and precipitation. *Mon. Wea. Rev.*, **144**, 3333–3354.

Zhang, J. A., and F. D. Marks, 2015: Effects of horizontal diffusion on tropical cyclone intensity change and structure in idealized three-dimensional numerical simulations. *Mon. Wea. Rev.,* **143**, 3981–3995.

Zhang, J. A., D. S. Nolan, R. F. Rogers, and V. Tallapragada, 2015: Evaluating the impact of improvements in the boundary layer parameterization on hurricane intensity and structure forecasts in HWRF. *Mon. Wea. Rev.,* **143**, 3136–3155.

Zhang, J. A., R. F. Rogers, and V. Tallapragada, 2017: Impact of parameterized boundary layer structure on tropical cyclone rapid intensification forecasts in HWRF. *Mon. Wea. Rev.*, **145**, 1413–1426.

Zhang, J. A., P. G. Black, J. R. French, and W. M. Drennan, 2008: First direct measurements of enthalpy flux in the hurricane boundary layer: the CBLAST results. *Geophys. Res. Lett.*, **35 (11)**, L14813, doi:10.1029/2008GL034374.

Zhang, J. A., S. G. Gopalakrishnan, F. D. Marks, R. F. Rogers, and V. Tallapragada, 2012: A developmental framework for improving hurricane model physical parameterization using aircraft observations, *Trop. Cycl. Res. Rev.*, **1 (4)**, 419–429.

Zhang, J. A., F. D. Marks, M. T. Montgomery, and S. Lorsolo, 2011a: An estimation of turbulent characteristics in the low-level region of intense hurricanes Allen (1980) and Hugo (1989). *Mon. Wea. Rev.*, **139**, 1447–1462.

Zhang, J. A., R. F. Rogers, D. S. Nolan, and F. D. Marks, 2011b: On the characteristic height scales of the hurricane boundary layer. *Mon. Wea. Rev.*, **139**, 2523–2535.

Zhu, P., K. Menelaou, and Z.-D. Zhu, 2014: Impact of subgrid-scale vertical turbulent mixing on eyewall asymmetric structures and mesovortices of hurricanes. *Quart. J. Roy. Meteor. Soc.*, **140**, 416–438.
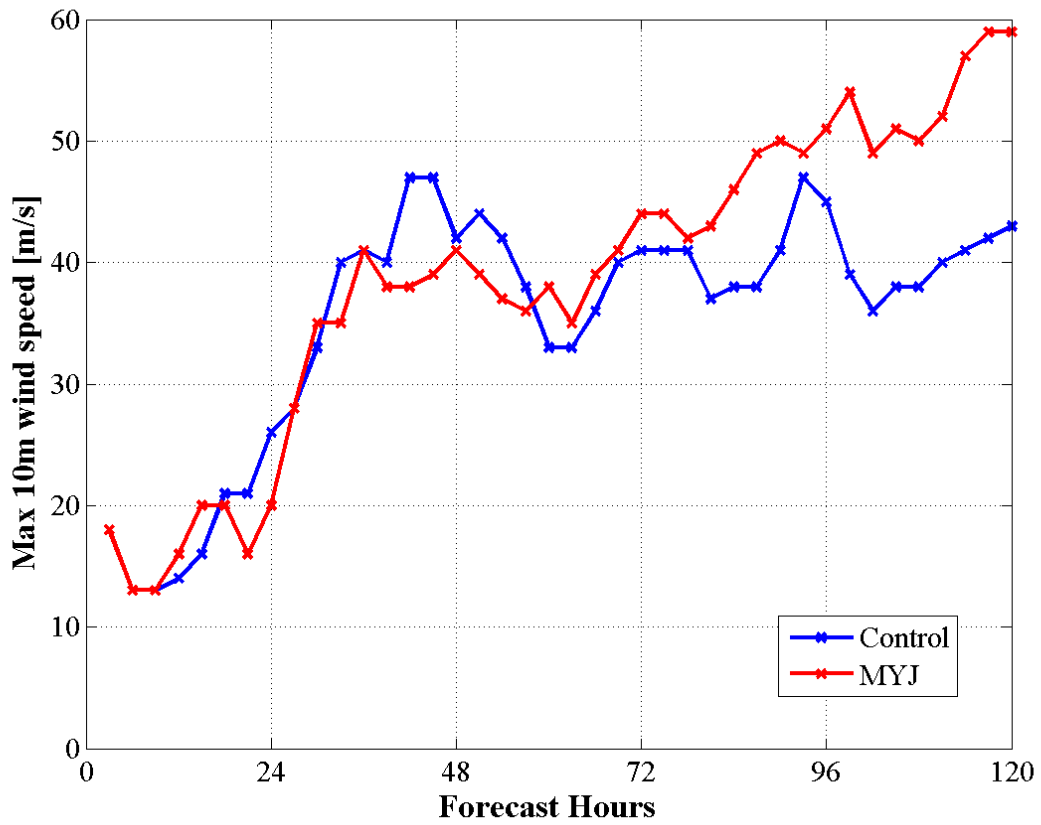
Figure 1: Plots of simulated storm intensity for the two idealized HWRF runs with different PBL schemes. The control experiment used the GFS scheme as in the HWRF model (V3.6).
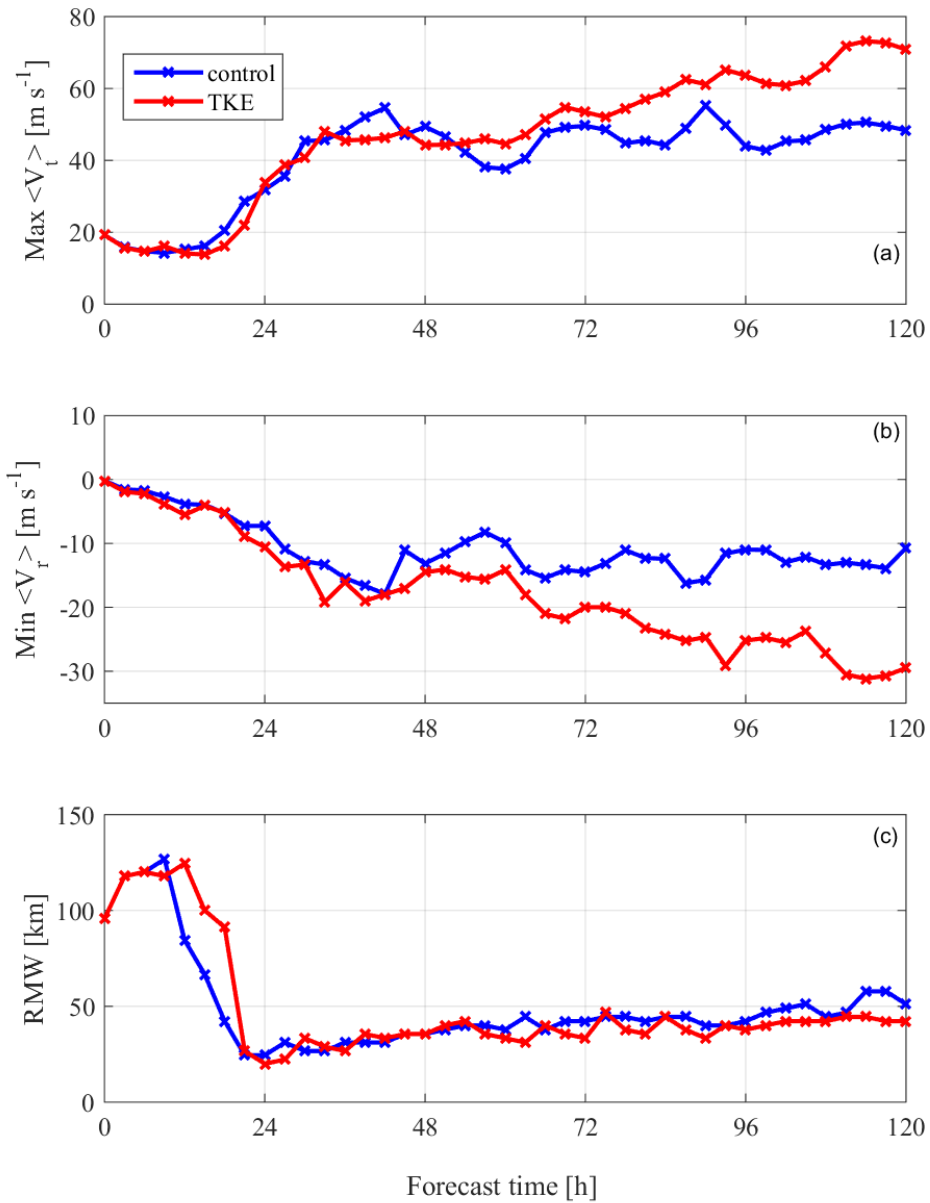
Figure 2: Plots of (a) the maximum azimuthally averaged tangential wind speed ($<Vt>$), (b) minimum azimuthally averaged radial wind speed ($<V_r>$), (c) radius of maximum wind speed at 2 km altitude as a function of forecast time for the control (blue) and TKE (red) simulations.
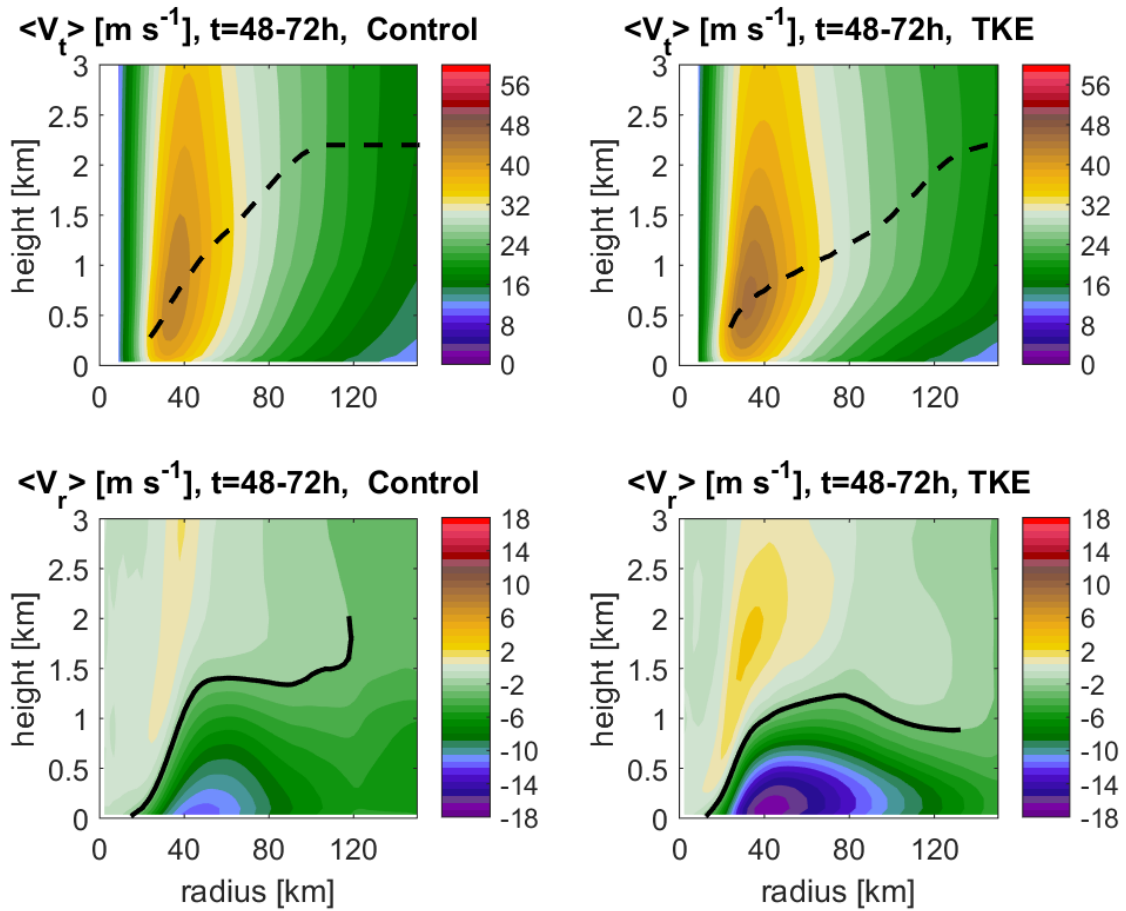
Figure 3: Radius-height plot of azimuthally averaged tangential (upper panels) and radial (lower panels) wind speed averaged during 48-72 h of forecasts for the control (left panels) and TKE (right panels) simulations. The black dashed line represents the height of the maximum tangential wind speed and the black solid line represents the inflow layer depth defined as the height of 10% peak inflow following Zhang et al. (2011).
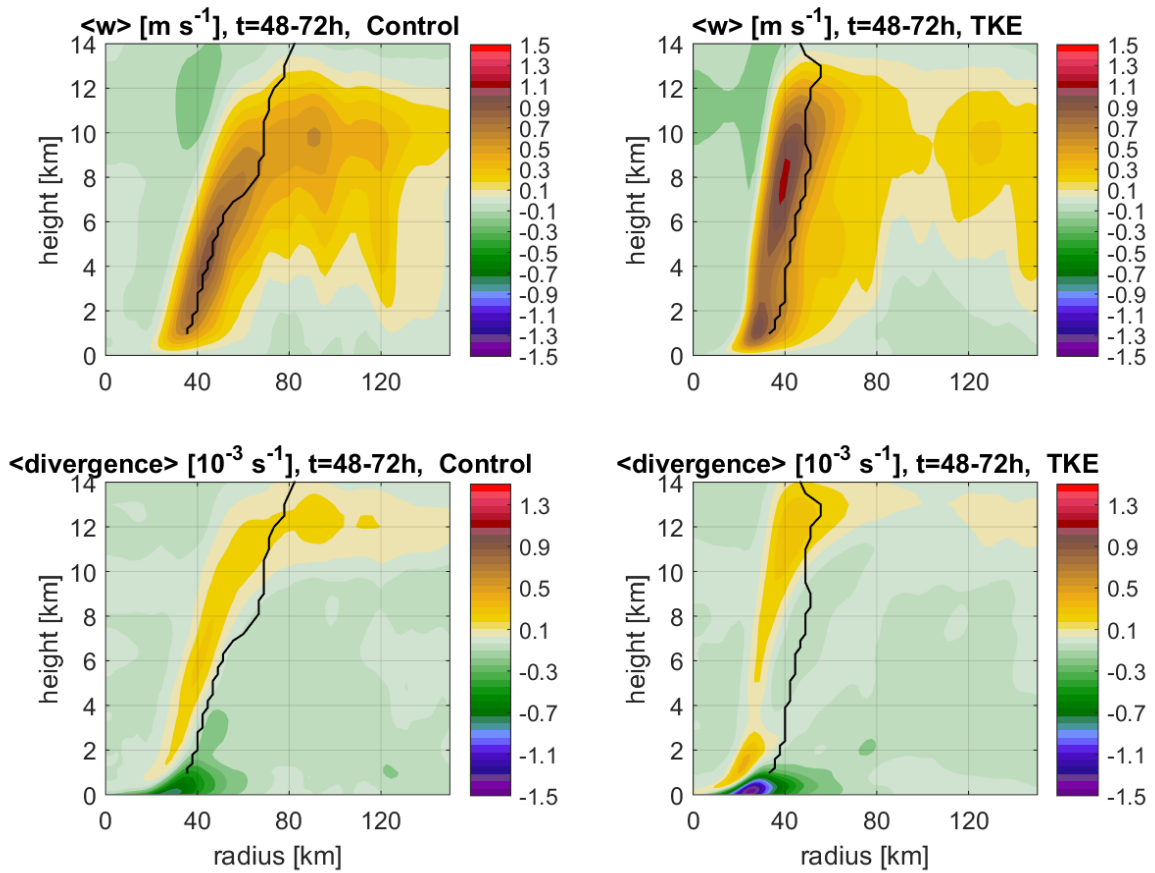
Figure 4: Radius-height plot of azimuthally averaged vertical velocity (upper panels) and divergence (lower panels) averaged during 48-72 h of forecasts for the control (left panels) and TKE (right panels) simulations. The black line represents the radius of maximum wind speed at each level.
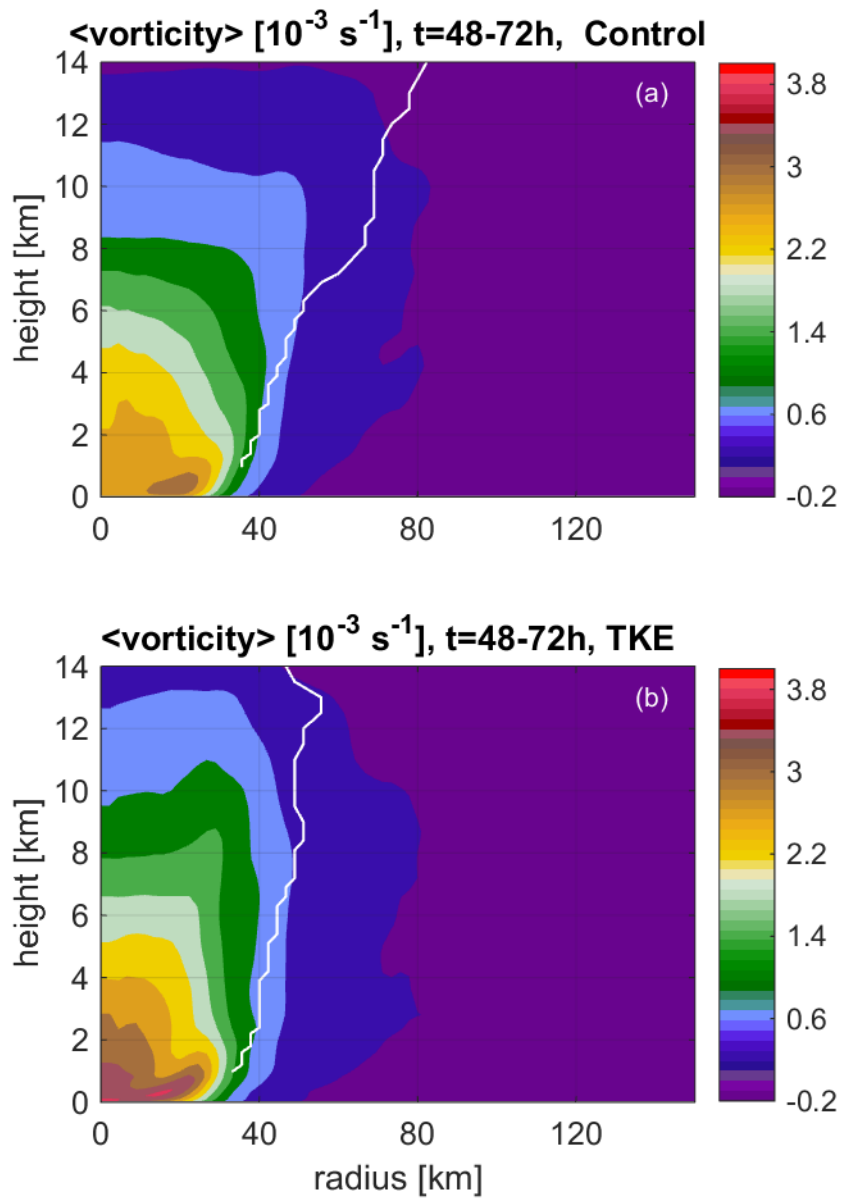
Figure 5: Radius-height plot of azimuthally averaged relative vorticity averaged during 48-72 h of forecasts for (a) control and (b) TKE simulations. The white line represents the radius of maximum wind speed at each level.
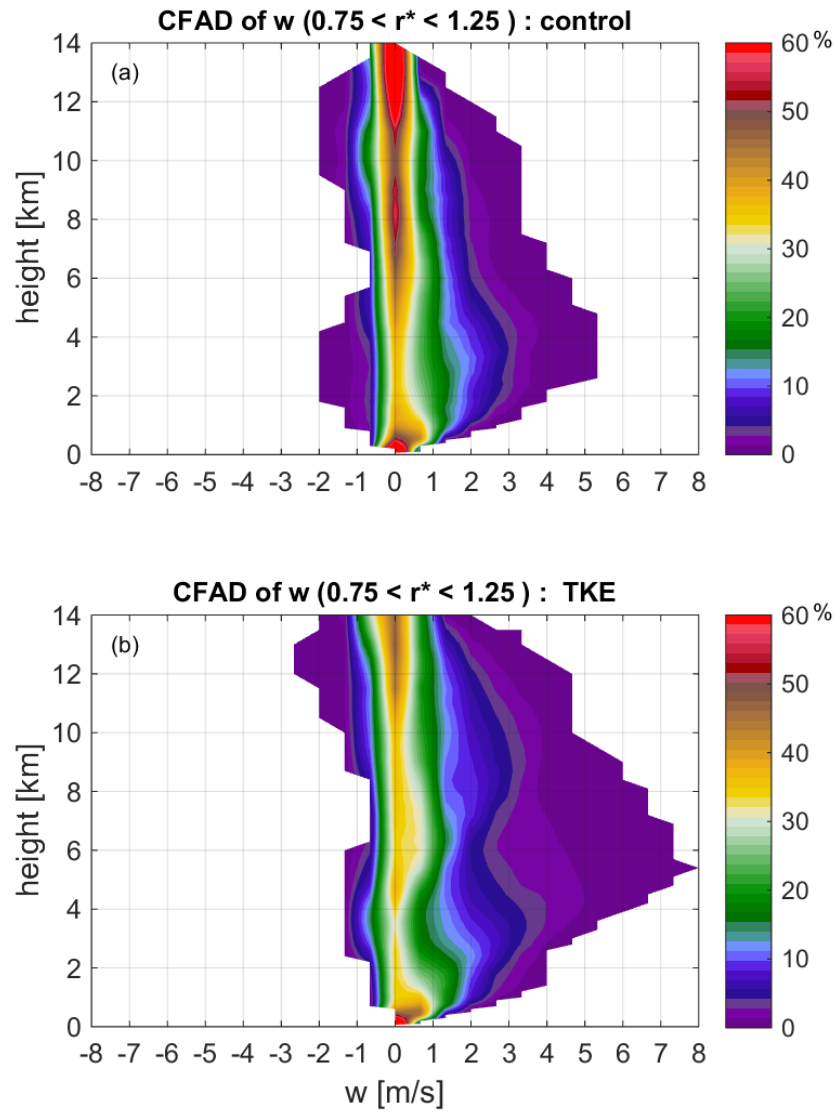
Figure 6: Contoured frequency by altitude (CFAD) diagram of the vertical velocity for the eyewall region (0.75r* < r < 1.25 r*) for (a) control and (b) TKE simulations.
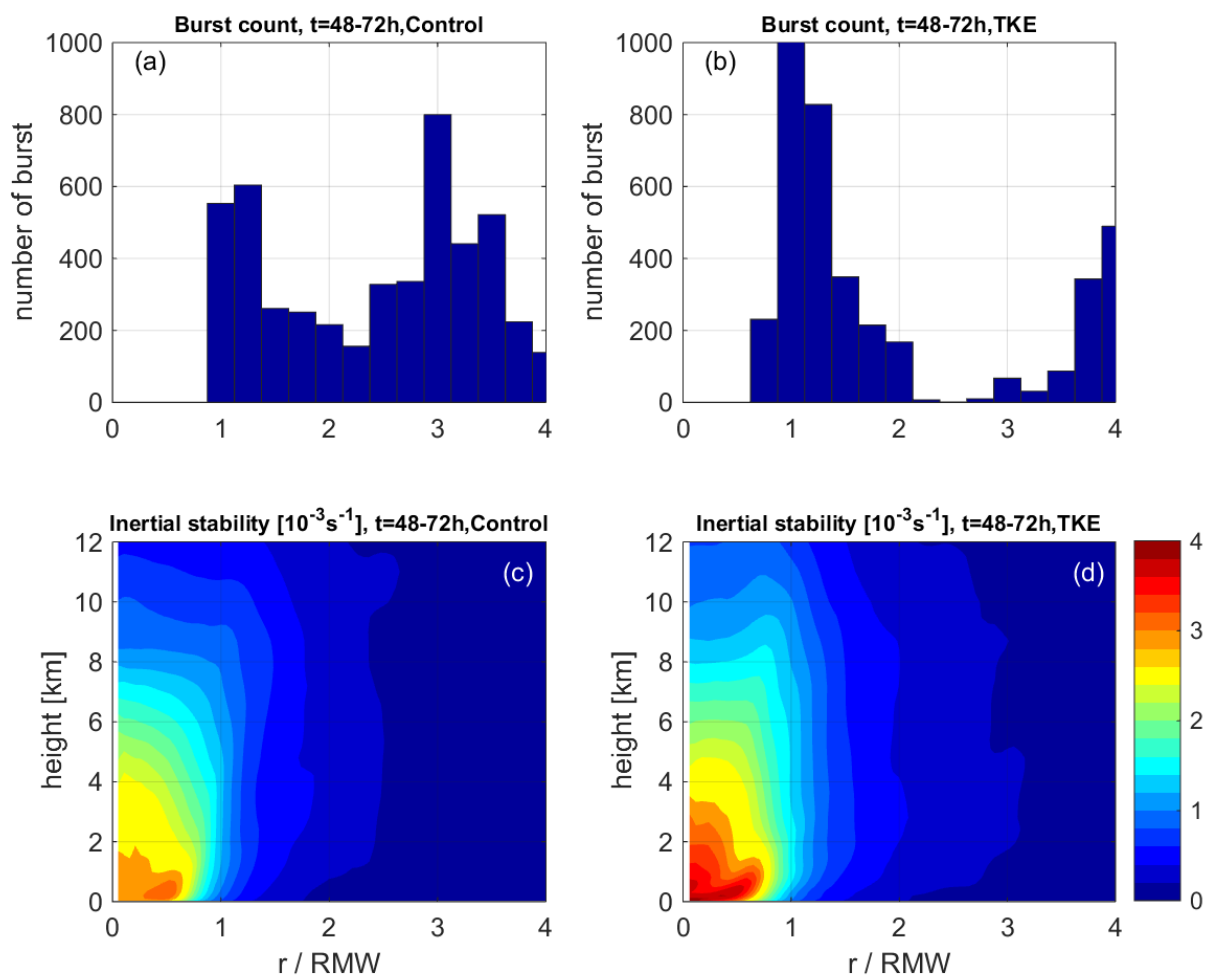
Figure 7: Plots of boundary layer heights as a function of forecast time.

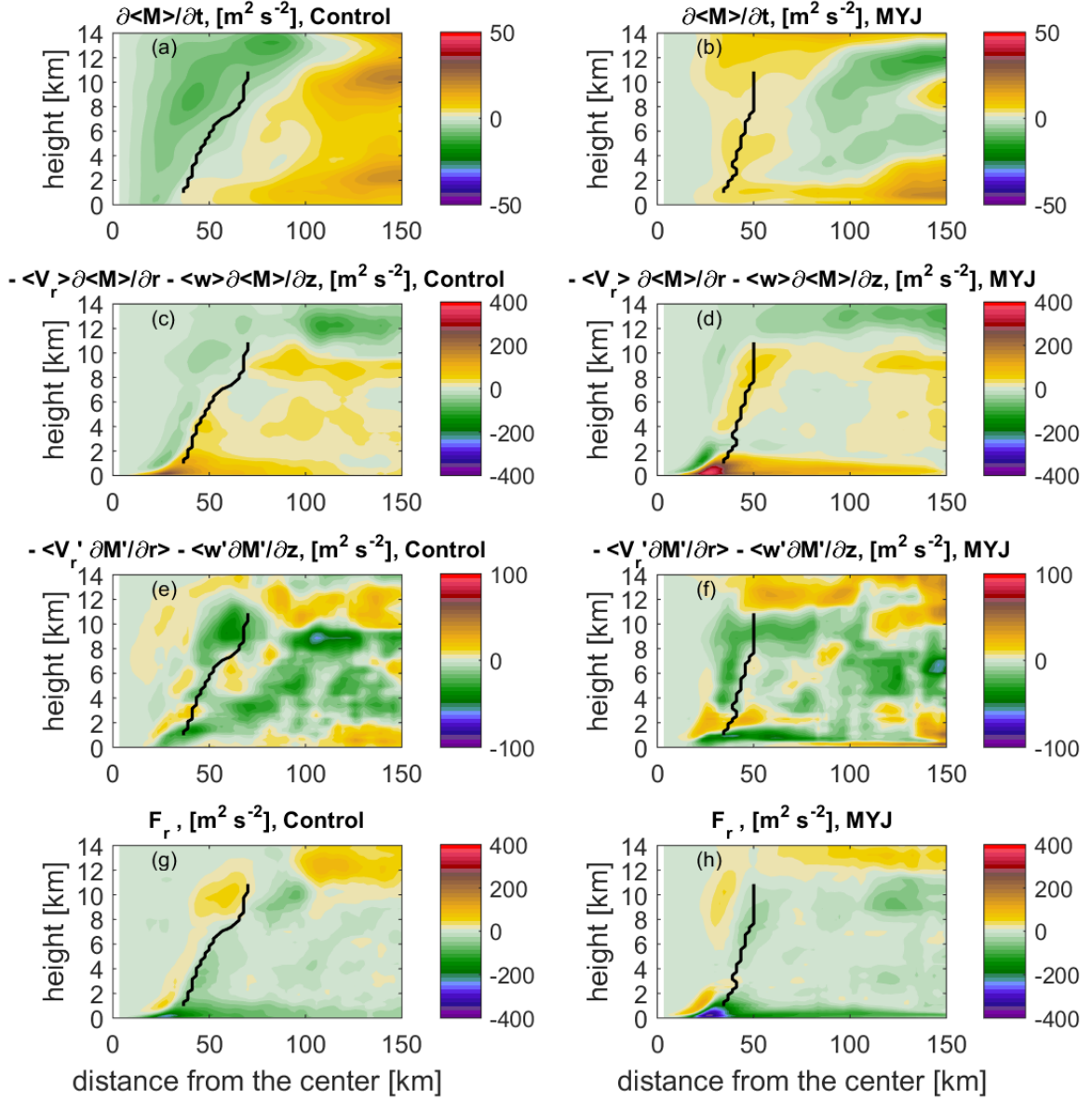**Figure 8:** Radius-height plots of the terms in the azimuthally-averaged absolute angular momentum (<*M*>) budget for simulations with the control run (left panels) and TKE run (right panels) during a period of rapid intensification (between 48-72 h). These budget terms include the local rate of change of (<*M*>) (a and b), the total mean advection (c and d), the sum of the eddy transport of (<*M*>) (e and f), and the friction term, F_r (g and h). The black line represents the radius of maximum azimuthally-averaged tangential wind speed.